

3-D seismic imaging in crystalline rock environments:

An approach based on diffraction focusing

K. A. Ahmed*, S. Dell†, B. Schwarz‡, D. Gajewski† & N. Ettrich*

** Fraunhofer Institute for Industrial Mathematics ITWM,*

Fraunhofer-Platz 1, 67663 Kaiserslautern, Germany

† Institute of Geophysics, University of Hamburg,

Bundesstr. 55, 20146 Hamburg, Germany

‡ Department of Earth Sciences, University of Oxford,

South Parks Road, Oxford OX1 3AN, United Kingdom

(April 10, 2019)

Running head: **Diffraction focusing in crystalline rocks**

ABSTRACT

Diffracted waves are seismic waves that backscatter from localized discontinuities in the earth. They describe backscattering from interfaces with either a curvature locally approaching infinity or occur if medium properties change on a scale smaller than the predominant seismic wavelength. Both types of diffracted events are of great importance in seismic processing as they allow to identify the presence of small inhomogeneities, truncations, faults, or pinch-out layers. However, to reliably interpret such subsurface features, diffractions should be properly imaged. An inherent part of the imaging is therefore a velocity model building tuned to diffractions. We present a method for 3-D velocity analysis based on the medium's diffraction response. We propose to evaluate a focusing norm along diffraction traveltimes in the time domain. The focusing analysis considers both amplitude and phase

of the diffracted events which results in several output volumes: three migration velocities for point diffractions, and one migration velocity and azimuth for edge diffractions. As additional information, the focusing analysis provides two coherence volumes which can be used to classify the back-scattering geology. Application of the proposed imaging strategy to 3-D seismic field data, acquired in the context of geothermal exploration in eastern Germany, reveals that crystalline rocks cause a rich diffraction response whose focusing can provide complementary insight into structures that are notoriously hard to image conventionally.

INTRODUCTION

Diffracted waves are seismic waves which, as well as reflected waves, describe a backscattering phenomenon from discontinuities in the earth. While specular reflected waves describe backscattering from a smooth interface with a size larger than the wavelength, and are fully covered by ray theory, diffracted waves appear as an extreme case where ray validity conditions are not satisfied. This is the case which describes backscattering from interfaces with either a curvature growing locally to infinite or a size much less than the wavelength. In the first case one usually speak of tip and edge diffractions, in the latter one about single scattering. An example of geological models producing edge diffractions are edges, corners or vertexes of boundary surfaces. Geological subsurface features producing point diffraction are small bodies or velocity agitation about the certain size of the first Fresnel zone, i.e., their size d , which is comparable to the apparent wavelength, λ , or with the radius of Fresnel zone R_f , so the relations $d \sim \lambda$, or $d \sim R_f$ hold (d is diameter). Note, depending on the seismic data, e.g., laboratory, reflection seismic, global seismology, the size d may vary from few millimeters (mm) to several of kilometers (km). The edge diffractions exhibit a phase reversal at their apex and have a directional-dependent response while single scatter radiates equally in any direction. Even if the dynamic properties of both backscattering types differ, their kinematic behavior remains the same, (see, e.g. , Klem-Musatov, 1994; Kravtsov and Zhu, 2010). Therefore, it is common to describe both backscattering phenomena as seismic diffractions.

Diffractions carry comprehensive information about the subsurface in regions of high interest for the reservoir characterization, modeling and exploitation. They provide a naturally and physically justified way for enhanced-resolution imaging beyond the classical

Rayleigh limit (Landa and Keydar, 1998; Khaidukov et al., 2004; Zhongxian et al., 2015). Moreover, the diffracted wavefield is determined mainly by properties of the medium in a small or nearby neighborhood of the scattering source (Moser and Howard, 2008; Protasov et al., 2016). Therefore, diffractions can be used to extract substantial velocity information in the nearest vicinity of the potential scatterer providing an illumination usually superior to reflections (Sava et al., 2005; Reshef and Landa, 2009; Bauer et al., 2017). In the poststack domain, diffractions can be used to calibrate velocity models, i.e., for residual moveout analysis (Coimbra et al., 2013). However, diffractions are inherently of 3-D nature (Rad et al., 2017). Thus, velocity analysis should be tuned to diffractions and consider three spatial dimensions. We propose to perform migration velocity analysis by evaluating a focusing norm along diffraction operators in the time domain. We compute the diffraction traveltimes using a poststack diffraction traveltime equation and parametrize it for point diffractions by three parameters: inline, crossline and 45 degrees velocity. For edge diffractions, we use a single velocity to determine the traveltime equation. The determined velocities can be used for an update of the existing velocity models as well as for the migration of the diffractions. As additional information, the proposed focusing analysis may be used to extract two coherence volumes which could further be used for interpreting seismic diffractions, i.e., to differentiate between different diffracting structures.

Crytalline rock environments, as they can be encountered in many continental regimes, such as e.g. in central Europe, typically cause diffuse and complicated wavefields and, therefore, are notoriously hard to image with conventional techniques (Milkereit et al., 2000; Eaton et al., 2003; Lay et al., 2016). Since areas of mining and, consequently, important natural resources such as Nickel or Copper, are commonly connected to hardrock formations, the development of novel imaging methodologies that can help to circumvent these natural

limitations are at the center of active ongoing research (e.g. Malehmir et al., 2012). In this work, we apply the aforementioned method for diffraction focusing to a 3-D seismic multi-channel dataset acquired in the context of geothermal exploration in Saxony, Germany – an area that is strongly dominated by the mid-German chrystalline zone. Building on previous studies by Lüschen and Schulz (2014), Hlousek et al. (2015), and Ahmed et al. (2015), performed in a scientific collaboration, we present results of diffraction focusing, which suggest that crystalline rocks indeed heavily diffract and that a complicated diffuse feature in the deeper crust is characterized by a noticeably higher rate of diffraction than its surroundings, painting a picture complementary to conventional techniques. This method is robust and results are better then coventional methods.

SEISMIC DIFFRACTIONS AND FOCUSING ANALYSIS

In the following, we present the theoretical foundation of our diffraction focusing workflow. As this scheme makes use of the often faint diffracted wavefield, as a first step, other interfering and more prominent wavefield components, such as reflections, have to be suppressed. While a wide variety of diffraction separation techniques appear in recent literature (e.g. Fomel et al., 2007; Dell and Gajewski, 2011; Klovov and Fomel, 2012; Schwarz and Gajewski, 2017) we here make use of an approach as suggested by (Zhang, 2005), whcih is based on a Radon transform. Focusing analysis represents a poststack coherence analysis, where one evaluates the coherence value along diffraction curves (see, e.g. Dell and Gajewski, 2011; Dell et al., 2013). As mentioned above point and edge diffractions differ in their dynamic properties. Amplitudes of point diffractions have no directional dependency while edge diffractions have a certain response signature. Figure 1a,b shows a hypothetic seismic experiment and an amplitude-versus-azimuth plot. The source, receiver and the azimuth are

mentioned in the figure. The most amplitudes will be recorded if the acquisition line is perpendicular to the surface projection of the fault. This allows to extract not only coherence values but also the midpoint (inline) azimuth.

[Figure 1 about here.]

For the diffracted events, we perform a simple velocity scan for a given azimuth as the shape of the diffracted curve is defined by a single moveout velocity. We define the summation window by two parameters: coherence radius, R , and aperture, A . The coherence radius R depends on the length of the signal. We also define a set of trial velocities. Therefore, we get a set of coherence values, $\{S\}_n$, corresponding to the trial velocity values, $\{V\}_n$. Afterwards, the velocity V_i corresponding to the maximum semblance S_i is chosen. We assign the value of S_i to corresponding (x, t) point building a coherence map. For point diffractions, we perform a velocity search based on a global optimization algorithm, differential evolution. Here, we simultaneously estimate three component of azimuth-dependent velocity.

Poststack coherence analysis for point diffraction in the time domain

First, we present an azimuth-dependent diffraction traveltimes operator. To do that, we introduce the unit direction vector $\mathbf{e}_\theta = (\cos \theta, \sin \theta)^T$ and examine the corresponding single-azimuth version of the diffraction operator in the azimuth direction $\mathbf{e}(\theta)$. More specifically, in midpoint and half-offset coordinates we set

$$\mathbf{m}(\theta) = \Delta m \mathbf{e}(\theta) \quad \text{and} \quad \mathbf{h}(\theta) = \Delta h \mathbf{e}(\theta) \quad (1)$$

where Δm and Δh are scalars staying for the midpoint and half-offset displacement with respect to the central ray. For the poststack case, $\Delta h = 0$ so that the diffraction operator

simplifies to

$$t[\mathbf{m}(\theta)]^2 = (t_0)^2 + 8t_0 \mathbf{e}(\theta)^T \mathbf{M} \mathbf{e}(\theta) \Delta m^2 . \quad (2)$$

where \mathbf{M} is a matrix containing wavefront curvatures of diffraction response.

Following Iversen and Tygel (2008) and in analogy with so-called NMO-ellipse of Grechka and Tsvankin (1998), the diffraction velocity, $v(\theta)$, along the single azimuth direction, $\mathbf{e}(\theta)$, satisfies the relationship

$$\begin{aligned} v(\theta)^2 &= \frac{2}{t_0 [\mathbf{e}(\theta)^T \mathbf{M} \mathbf{e}(\theta)]} \\ &= \frac{2}{t_0 [M_{11} \cos^2 \theta + M_{22} \sin^2 \theta + 2M_{12} \sin \theta \cos \theta]} . \end{aligned} \quad (3)$$

In particular, the diffraction velocities in the directions $\mathbf{e}(0) = (1, 0)^T$ (inline), and $\mathbf{e}(\pi/2) = (0, 1)^T$ (crossline) are, respectively, given by the diagonal elements of the matrix \mathbf{M} , namely,

$$v(0)^2 = \frac{2}{t_0 M_{11}} \quad \text{and} \quad v(\pi/2)^2 = \frac{2}{t_0 M_{22}} . \quad (4)$$

Poststack coherence analysis for edge diffraction in the time domain

Equation 3 defines migration velocities for point diffractions, where there is no directional dependency in the response. For diffracted events, we can consider the directional dependency of the response, so that the equation 2 simplifies to

$$t(\mathbf{m})^2 = t_0^2 + 8t_0 M \Delta m^2 , \quad (5)$$

which leads to the following definition for the migration velocity

$$v^2 = \frac{2}{t_0 M} . \quad (6)$$

Synthetic example

In this section, we show applications of the presented method for diffraction imaging to synthetic data examples.

[Figure 2 about here.]

[Figure 3 about here.]

[Figure 4 about here.]

[Figure 5 about here.]

The model, model B, consists of a homogeneous layer where a box-like structure is embedded (Figure 2(c)). The velocity in the layer is 1700 m/s. The velocity in the box is 2000 m/s. This edge of the box causes edge diffractions which have the phase change at the diffraction apexes since an edge diffraction must undergo a phase change of 180 degrees (Torey, 1970). Seismograms are generated using the same settings as for model A. Five lines of the 3-D stacked volume are displayed in Figure 3(b)a.

We also use the stacked volume for migration velocity analysis. First, the time migration velocity analysis is applied to the diffractions. However, the phase change at the apex position distorts the conventional semblance analysis resulting in two foci near the diffraction apex. Therefore, we modified the velocity analysis as suggested by (Landa et al., 1987) to account for the phase change in the stacked volume. As a coherence measure we use

$$S = \frac{1}{M} \frac{\sum_t \left(\sum_{i=1}^M \pm f_{i,t(i)} \right)^2}{\sum_t \sum_{i=1}^M f_{i,t(i)}^2}, \quad (7)$$

where the plus sign is chosen for traces located in the 'off reflector' area and the minus sign for traces located in the 'on reflector' area. As we see in Figure 3(b) the phase change occurs for the trace located directly above the diffracting edge. Figure 6(a) shows a time-migration velocity panel for a CMP which is directly above the diffracting edge. We observe a good focusing though worse than for the model A data. This is because a point diffractor scatters in any direction, i.e., more traces are involved in the coherence measure, while edge diffractions exhibit a directional dependency. Figure 6(c) shows the coherence distribution of a time slice at 0.8 s in the X and Y direction. We observe that the coherence maximum coincides with the lateral position of the diffracting edge.

[Figure 6 about here.]

Figure 6(b) shows a depth-migration velocity panel for a CMP which is directly above the diffraction apex. We observe a reasonable semblance value but less focused image as in the time-migration analysis. Figure 6(d) shows the coherence distribution of a depth slice at 700 m in the X and Y direction. We see that the coherence maximum coincides with the lateral position of the edge but more smeared than in the time-migration velocity analysis.

CRYSTALLINE ROCK FIELD DATA APPLICATION

As field data example we use Schneeberg 3D seismic data set which represents sparsely sampled data with poor signal-to-noise ratio from a hard rock environment. The area is located in SE of Germany near the Czech border. This region comprises a complex tectonic regime. Compared to sedimentary environment, the signal quality is low in this dataset (Schreiter et al., 2015). The Schneeberg site is located in the southern basin which is known to be the Saxothuringian basin (figure 7). The tectonic setting of this area is

as shown (figure 8). The geological setting of the surface map shows lithology in different colours (figure 9). The important lithology includes yellow coloured inclined clayey schist which was the most reflecting feature of the study block (see Ahmed et al., 2015). The other distinguishing prominent body from the surface geology are the granitic intrusions (red colour) and regional fault Roter Kamm. A detailed description of the local geology can be found in Lüschen et al. (2015). In the map the northern part brown colour shows the Permian sediments. The detailed geology is available on map. Its origin goes back to an important Cambro-Ordovician phase of rifting, which is detectable almost everywhere in Europe (e.g. Emmermann et al., 1991).

The structure and tectonics of the study area include the number of low, medium and high grade igneous and metamorphic rock units whereas there is also some contrast of the sedimentary environment in the vicinity of this area. The regional tectonic zone is shown (figure 8 where the complexity of the region can be imagined. The area is a highly fractured zone with steep dipping tectonics from 60-70 degree of reflectors in upper part (Harjes et al., 1997). At the surface the area is characterized by faults. The shallow structure exhibit the inclined layers of metamorphosed rocks.

[Figure 7 about here.]

[Figure 8 about here.]

[Figure 9 about here.]

Seismic imaging in crystalline rock is not easy and straightforward because of the low acoustic impedance (e.g. Milkereit et al., 2000; Eaton et al., 2003; Malehmir et al., 2012). The output of this test gives a new way to look and interpret sparsely sampled data with low

signal-to-noise ratio from a hard rock environment. The maximum coherence of the signal here is 0.02. The ZO based seismic sections/volume gives more information regarding the subsurface structure as compared to the conventional CMP stacking method (Ahmed et al., 2015). The results were quite promising for the case where there is low reflectivity in this type of subsurface lithology. We can see the steeply dipping reflectors and steep faulting or deep reflections. Other than this, there is a fractured zone near 2000ms TWT the the geographic position of in-line 390 and cross-line 300. In the frame of the connected scientific collaboration – du to the proximity of the German town *Schneeberg*, this fractured zone was commonly referred to as the *Schneeberg body*. This is most prominent body as interesting part of this zone which was not expected by geologists prior to the surveys and it was never reported in past literatures. This feature might have evolved because of the steeply dipping and tectonically dominant regional fault *Roter Kamm* and the dipping clayey schist which cross-cut in deeper part. This is because of the compressional tectonic regime.

[Figure 10 about here.]

[Figure 11 about here.]

[Figure 12 about here.]

[Figure 13 about here.]

[Figure 14 about here.]

[Figure 15 about here.]

The figure 11 shows the result of the crs-stacked volume. In this image we have observed the reflectors with some micro-tectonic structures like the fractured zone (*Schneeberg body*).

There is some fracturing seems to be in the upper part of the seismic volume which are conjugate faults. The conjugate faults seems to be mineralized. In figure 12 the features seems to be clear and more understandable and easily interpretable. The lithology seems to be highly fractured due to the compressional tectonic regime. The Common-Reflection-Surface-Stacked volume is final stacked volume before the migration. The results of this migration are quite promising and it is visible from images. Figure 13 and 14 show the position of the most diffracted part of the study block. Out of the cube, the selected slices of inline and cross-line shows that clusters show the diffraction points as the apex position. The images look promising as they have focussed well diffractions and show the potential prospect zone of the volume. This clustered accumulation of diffractions give the position of the highly fractured zone as in figure 15. The 3D model gives inside of the subsurface the real position of diffractions. The red flag shows the initial decided drill place proposed before the survey has been done. This study could lead to the modeling and reservoir characterization as the fractured zones are of great interest for exploration scientists.

DISCUSSION

The presented 3-D field data example from a crystalline environment near Schneeberg, Germany, reconfirms that recorded seismic wavefields are complicated, with diffraction representing arguably an important ingredient. Consequently, owing to this complexity, conventional reflection-based processing was found to be well-complemented by the targeted focusing of diffractions. Due to the diffuse character of the observed wavefields, coherence analysis, such as the common-reflection-surface (CRS) workflow, may result in improved data quality, but the extracted and derived attributes, including migration velocities, might be compromised and inaccurate. However, it can be argued that all processes that im-

prove the S/N ratio of the prestack data intrinsically have a positive impact on subsequent processing steps including migration. The partial CRS stack introduced by Baykulov and Gajewski (2009) and subsequently generalized by Xie and Gajewski (2017) as well as the 3-D prestack diffraction separation and imaging workflow by Rad et al. (2018) might be considered in the near future. Since conventional CRS implementations incorporate a hyperbolic traveltimes approximation, diffractions might better be described by double-square-root-type descriptions (e.g. Landa et al., 2010; Fomel and Kazinnik, 2013; Schwarz et al., 2014).

Another approach of pre-stack data (signal) enhancement is the partial time migration introduced by Dell et al. (2012). This tool also has an ability to improve the seismic signal quality and demands only reasonable migration velocities in time domain to be applied effectively. 3D normal-incidence-point (NIP) wave tomography (Duveneck, 2004b,a) can be used to approximate the velocity model using the attributes by automatic or manual picking of reliable events. Anisotropy is one of the major goals which can assist in improvement of such type of datasets. Depending on the dataset at hand, other potentially more flexible diffraction separation techniques, as e.g. introduced by Schwarz and Gajewski (2017) can be considered. As can be inferred from e.g. Figure 11 conflicting dips are a main issue in CRS-type processing and for accurate and artefact-free subsequent migration. need to be accounted for. The method proposed by Walda and Gajewski (2017) can be implemented for the 3-D case to solve this problem. As the data is dominated by diffractions, a specialized processing and tomography technique recently discussed by Schwarz et al. (2016) and Bauer et al. (2017) may rail to a new recipe for velocity model estimation entirely based on zero-offset data.

CONCLUSIONS

We have presented a method to image diffractions in three dimensions. The first step in our approach is the attenuation of reflected events using kinematic wavefield attributes. The separated diffracted events are then used for migration velocity analysis using diffraction traveltimes. The separation of diffracted events in three dimensions is performed using kinematic wavefield attributes determined by the CRS approach. The isolated diffracted events were used for a poststack time and depth domain migration velocity model building. The velocity analysis consists of a velocity scan and the estimation of the corresponding semblance norm for each sample in the poststack volume or grid point in the depth domain, respectively. In the poststack domain, the data are considerably reduced in size and a good S/N ratio is present. The computational efficiency of analytic traveltime calculations combined with the speed and low cost of current high performance computing techniques allow a very fast and robust initial depth-migration velocity analysis. Synthetic data examples demonstrate that the presented method leads to focused images of diffracted events in time and depth. Subsequent application of the workflow to 3-D crystalline rock field data from eastern Germany suggests that diffraction is a prevalent phenomenon in these environments and should not be ignored, as it provides complementary information, which is especially important in situations, where conventional reflection-based seismic imaging fails.

ACKNOWLEDGEMENTS

We would like to thank the Federal Ministry of Economic Affairs and Energy (BMWi), Germany for partially funding this research (0325363A). We thank the sponsors of the Wave Inversion Technology (WIT) consortium for support. Discussions with project partners from

LIAG, Hannover and TU Freiberg as well as fruitful discussions with in the Applied Seismics group, Hamburg are likewise appreciated. We are grateful to Ekkehart Teßmer for providing the modelling software used in the frame of this study, as well as to Dela Spickermann and Michael Böttinger of the German Climate Computing Centre (DKRZ) for support in terms of allocated computing time and data visualization. BS acknowledges support by the German Research Foundation (DFG, SCHW 1870/1-1).

REFERENCES

- Ahmed, K., B. Schwarz, and D. Gajewski, 2015, Application of the 3D common-reflection-surface stack workflow in a crystalline rock environment: *Geophysical Prospecting*, **63**, 990–998.
- Bauer, A., B. Schwarz, and D. Gajewski, 2017, Utilizing diffractions in wavefront tomography: *Geophysics*, **82**, R65–R73.
- Baykulov, M., and D. Gajewski, 2009, Prestack seismic data enhancement with partial common-reflection-surface (CRS) stack: *Geophysics*, **74**, V49–V58.
- Coimbra, T., J. de Figueiredo, J. Schleicher, A. Novais, and J. Costa, 2013, Migration velocity analysis using residual diffraction moveout in the poststack depth domain: *Geophysics*, **78**, S125–S135.
- Dell, S., and D. Gajewski, 2011, Common-reflection-surface-based workflow for diffraction imaging: *Geophysics*, **76**, S187–S195.
- Dell, S., D. Gajewski, and C. Vanelle, 2012, Prestack time migration by common-migrated-reflector-element stacking: *Geophysics*, **77**, S73–S82.
- Dell, S., A. Pronevich, B. Kashtan, and D. Gajewski, 2013, Diffraction traveltime approximation for general anisotropic media: *Geophysics*, **78**, WC15–WC23.
- Duveneck, E., 2004a, 3D tomographic velocity model estimation with kinematic wavefield attributes: *Geophysical Prospecting*, **52**, 535–545.
- , 2004b, Velocity model estimation with data-derived wavefront attributes: *Geophysics*, **69**, 265–274.
- Eaton, D., B. Milkereit, and M. Salisbury, 2003, Seismic methods for deep mineral exploration: Mature technologies adapted to new targets: *The Leading Edge*, **22**, 580–585.
- Emmermann, R., A. Duba, and J. Lauterjung, 1991, Super-deep, continental drilling in

- Germany: Eos, Transactions American Geophysical Union, **72**, 193–197.
- Fomel, S., and R. Kazinnik, 2013, Non-hyperbolic common reflection surface: Geophysical Prospecting, **61**, 21–27.
- Fomel, S., E. Landa, and M. Taner, 2007, Poststack velocity analysis by separation and imaging of seismic diffractions: Geophysics, **72**, U89–U94.
- Grechka, V., and I. Tsvankin, 1998, 3-D description of normal moveout in anisotropic inhomogeneous media: Geophysics, **63**, 1079–1092.
- H. J. Berger, H. J., S. Felix, M. and Görne, E. Koch, O. Krentz, A. Förster, H. J. Förster, H. Konietzky, C. Lunow, K. Walter, H. Schütz, K. Stanek, and S. Wagner, 2011, Tiefengeothermie Sachsen.
- Harjes, H.-P., K. Bram, H.-J. Dürbaum, H. Gebrande, G. Hirschmann, M. Janik, M. Klöckner, E. Lüschen, W. Rabbel, M. Simon, et al., 1997, Origin and nature of crystal reflections: Results from integrated seismic measurements at the KTB superdeep drilling site: Journal of Geophysical Research: Solid Earth, **102**, 18267–18288.
- Hlousek, F., O. Hellwig, and S. Buske, 2015, Three-dimensional focused seismic imaging for geothermal exploration in crystalline rock near Schneeberg, Germany: Geophysical Prospecting, **63**, 999–1014.
- Iversen, E., and M. Tygel, 2008, Image-ray tracing for joint 3D seismic velocity estimation and time-to-depth conversion: Geophysics, **73**, S99–S114.
- Khaidukov, V., E. Landa, and T. Moser, 2004, Diffraction imaging by focusing-defocusing: An outlook on seismic superresolution: Geophysics, **69**, 1478–1490.
- Klem-Musatov, K., 1994, Theory of seismic diffractions: Society of Exploration Geophysicists.
- Klokov, A., and S. Fomel, 2012, Separation and imaging of seismic diffractions using mi-

- grated dip-angle gathers: *Geophysics*, **77**, S131–S143.
- Kravtsov, Y., and N. Zhu, 2010, *Theory of diffraction. Heuristic approaches*: Alpha Science International.
- Landa, E., and S. Keydar, 1998, Seismic monitoring of diffraction images for detection of local heterogeneities: *Geophysics*, **63**, 1093–1100.
- Landa, E., S. Keydar, and T. J. Moser, 2010, Multifocusing revisited-inhomogeneous media and curved interfaces: *Geophysical Prospecting*, **58**, 925–938.
- Landa, E., V. Shtivelman, and B. Gelchinsky, 1987, A method for detection of diffracted waves on common-offset sections: *Geophysical Prospecting*, **35**, 359–373.
- Lay, V., S. Buski, A. Lukács, A. R. Gorman, S. Bannister, and D. R. Schmitt, 2016, Advanced seismic imaging techniques characterize the Alpine Fault at Whataroa (New Zealand): *Journal of Geophysical Research: Solid Earth*, **121**, 8792–8812.
- Linnemann, U., 2010, Pre-Mesozoic geology of Saxo-Thuringia: From the Cadomian active margin to the Variscan orogen: *Schweizerbart*.
- Lüschen, E., S. Görne, H. von. Hartmann, R. Thomas, and R. Schulz, 2015, 3D seismic survey for geothermal exploration in crystalline rocks in saxony, germany: *Geophysical Prospecting (Special Issue Hardrock)*.
- Lüschen, E., and R. Schulz, 2014, 3-D Seismic Surveys Explore German Petrothermal Reserves: *EOS Transactions, American Geophysical Union*, **95**, 237–244.
- Malehmir, A., R. Durrheim, G. Bellefleur, M. Urosevic, C. Juhlin, D. White, B. Milkereit, and G. Campbell, 2012, Seismic methods in mineral exploration and mine planning: A general overview of past and present case histories and a look into the future: *Geophysics*, **77**, WC173–WC190.
- Milkereit, B., E. Berrer, A. King, A. Watts, B. Roberts, A. Erick, D. Eaton, J. Wu, and M.

- Salisbury, 2000, Development of 3-D seismic exploration technology for deep nickel-copper deposits—A case history from the Sudbury basin, Canada: *Geophysics*, **65**, 1890–1899.
- Moser, T. J., and C. B. Howard, 2008, Diffraction imaging in depth: *Geophysical Prospecting*, **56**, 627–641.
- Protasov, M. I., G. V. Reshetova, and V. A. Tcheverda, 2016, Fracture detection by Gaussian beam imaging of seismic data and image spectrum analysis: *Geophysical Prospecting*, **64**, 68–82.
- Rad, P., , D. Gajewski, and L. Macelloni, 2018, Diffraction separation based on the projected first Fresnel zone: *Journal of Geophysics and Engineering*, **15**, 2507–2515.
- Rad, P., B. Schwarz, D. Gajewski, and C. Vanelle, 2017, Common-reflection-surface-based prestack diffraction separation and imaging: *Geophysics*, **83**, S47–S55.
- Reshef, M., and E. Landa, 2009, Post-stack velocity analysis in the dip-angle domain using diffractions: *Geophysical Prospecting*, **57**, 811–821.
- Sava, P., B. Biondi, and J. Etgen, 2005, Wave-equation migration velocity analysis by focusing diffractions and reflections: *Geophysics*, **70**, U19–U27.
- Schreiter, L., F. Hloušek, O. Hellwig, and S. Buske, 2015, Characterization of seismic reflections from faults in a crystalline environment, Schneeberg, Germany: *Geophysical Prospecting*, **63**, 1015–1032.
- Schwarz, B., A. Bauer, and D. Gajewski, 2016, Passive seismic source localization via common-reflection-surface attributes: *Studia Geophysica et Geodaetica*, **60**, 531–546.
- Schwarz, B., and D. Gajewski, 2017, Accessing the diffracted wavefield by coherent subtraction: *Geophysical Journal International*, **211**, 45–49.
- Schwarz, B., C. Vanelle, D. Gajewski, and B. Kashtan, 2014, Curvatures and inhomogeneities: An improved common-reflection-surface approach: *Geophysics*, **79**, S231–S240.

- Trorey, A. W., 1970, A simple theory for seismic diffractions: *Geophysics*, **35**, 762–784.
- Walda, J., and D. Gajewski, 2017, Determination of wavefront attributes by differential evolution in the presence of conflicting dips: *Geophysics*, **82**, V229–V239.
- Xie, Y., and D. Gajewski, 2017, 5-D interpolation with wave-front attributes: *Geophysical Journal International*, **211**, 919–941.
- Zhang, R., 2005, Imaging the earth using seismic diffractions by means of Radon transform: CSEG National Convention, Expanded Abstracts, 2293–2296.
- Zhongxian, L., W. Fengjiao, and D. Wang, 2015, The multi-domain FMM-IBEM to model elastic wave scattering by three-dimensional inclusions in infinite domain: *Engineering Analysis with Boundary Elements*, **60**, 95–105.

LIST OF FIGURES

1	A hypothetical seismic experiment and corresponding response signature (adapted from Klem-Musatov, 1994). Amplitudes decay depending on the midpoint (inline) azimuth. The strongest amplitudes will be recorded if the acquisition line is perpendicular to the surface projection of the fault.	22
2	(a) Model A: A simple geological model which consists of two layers and four diffractors. The velocity in the first layer is 1700 m/s, and in the second layer it is 2000 m/s. Diffractors are simulated with the velocity of 1700 m/s at four grid point. (b) Acquisition map. Shots are located along the five lines. Receivers are distributed over the whole acquisition area. Four black dots indicate the surface projection of the point diffractors. Three diffractors are located directly below line C. The fourth point diffractor is located transverse to line E. (c) Model B: The model represents a homogeneous layer where a box-like structure is embedded. The velocity in the box is 2000 m/s. The velocity in the surrounding layer is 1700 m/s. The edge of the box generates an edge diffraction.	23
3	A set of two subfigures.	24
4	A set of four subfigures.	25
5	A set of four subfigures.	26
6	A set of four subfigures.	27
7	Sketch illustrating the geographic location of the study area (denoted by a red star) close to the czech border. The 3-D seismic dataset was acquired in the context of a geothermal exploration campaign near a small town called Schneeberg.	28
8	Tectonic map of Saxothuringian zone hinting at the overall structural complexity of the area under investigation. Aside from different localized units, the mid-German crystalline zone outcrops in the north of the acquisition (whose location is sketched by a red frame). Linnemann (2010)	29
9	Geological map of the outcropping geology in the study area. Different colors indicate the different present geological units and a richness in fault systems is indicated by straight black lines. A main fault cutting through these formations (called <i>Roter Kamm</i>) is denoted by an arrow. H. J. Berger et al. (2011)	30
10	Time slice of the common-reflection-surface (CRS) stack (Ahmed et al., 2015). Arrows indicate the comparably strong signatures of the conjugate fault system known from outcrops related to mining and an apparently strongly diffracting structure (<i>Schneeberg body</i>).	31
11	Inline 390 of the common-reflection-surface (CRS) stack of the 3D seismic dataset acquired for geothermal exploration (compare Ahmed et al., 2015). Like in Figure 10 both, the reflective likely mineralized conjugate fault structures and the seemingly highly diffractive <i>Schneeberg body</i> are clearly distinguishable.	32

12	Maximized coherence achieved in the common-reflection-surface (CRS) workflow, indicating that aside from clearly distinguishable reflections caused by the minarized faults near the surface, a stong variety of weak but coherent conflicting contributions could be detected throughout the dataset.	33
13	Result of the proposed data-driven diffraction focusing analysis shown for the central inline 390 (compare 11). Localized coherence peaks correspond to diffracted events focused at their apices.	34
14	Exemplary crossline result (shown is crossline 300) of the suggested coherence-based scheme for diffraction focusing (compare Figure 13).While some noticable diffractivity could be detected close to the surface, a majority of focussed energy seems to be related to the <i>Schneeberg body</i> structure.	35
15	Full 3D visualization of the diffraction focusing achieved through the proposed workflow (low semblance values are transparent). While an overall diffractivity of the crystalline rocks can be observed, a higher diffraction rate in the location of the <i>Schneeberg body</i> hints at this structure’s intrinsic complexity. .	36

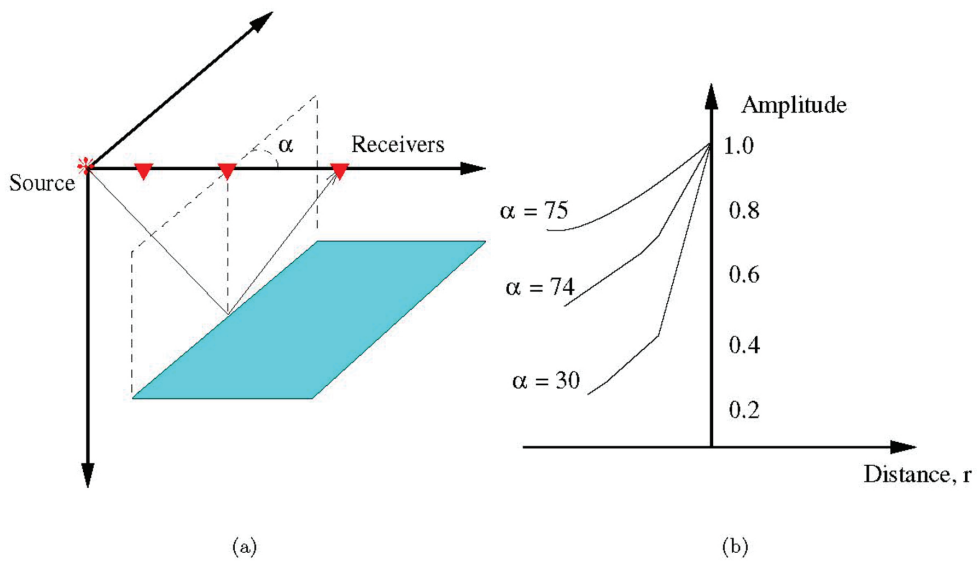


Figure 1: A hypothetical seismic experiment and corresponding response signature (adapted from Klem-Musatov, 1994). Amplitudes decay depending on the midpoint (inline) azimuth. The strongest amplitudes will be recorded if the acquisition line is perpendicular to the surface projection of the fault.

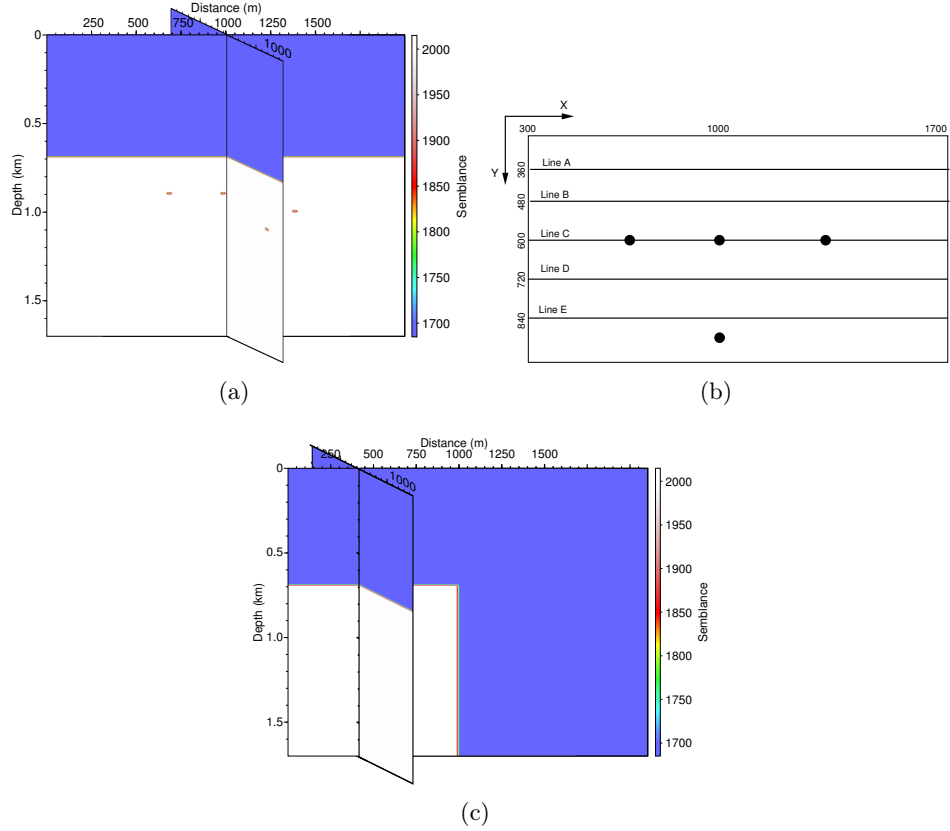


Figure 2: (a) Model A: A simple geological model which consists of two layers and four diffractors. The velocity in the first layer is 1700 m/s, and in the second layer it is 2000 m/s. Diffractors are simulated with the velocity of 1700 m/s at four grid point. (b) Acquisition map. Shots are located along the five lines. Receivers are distributed over the whole acquisition area. Four black dots indicate the surface projection of the point diffractors. Three diffractors are located directly below line C. The fourth point diffractor is located transverse to line E. (c) Model B: The model represents a homogeneous layer where a box-like structure is embedded. The velocity in the box is 2000 m/s. The velocity in the surrounding layer is 1700 m/s. The edge of the box generates an edge diffraction.

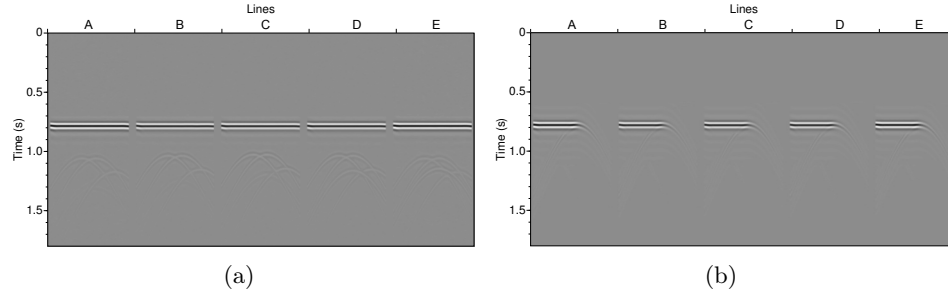


Figure 3: (a) Five vertical profiles of the 3-D stacked volume are displayed for model A. Profiles along lines A-E are shown. No amplitude gain is applied to the sections. We observe that the diffraction amplitudes are much weaker than the reflection ones and are hardly visible. (b) The stacked volume for the model B. Five vertical profile out of the 3-D volume are displayed with the same spatial coordinates as for model A. We observe that the diffraction amplitudes are again much weaker than the reflection ones and achieve their maxima at the diffracting edge. The phase reversal at the diffraction apexes is hardly visible.

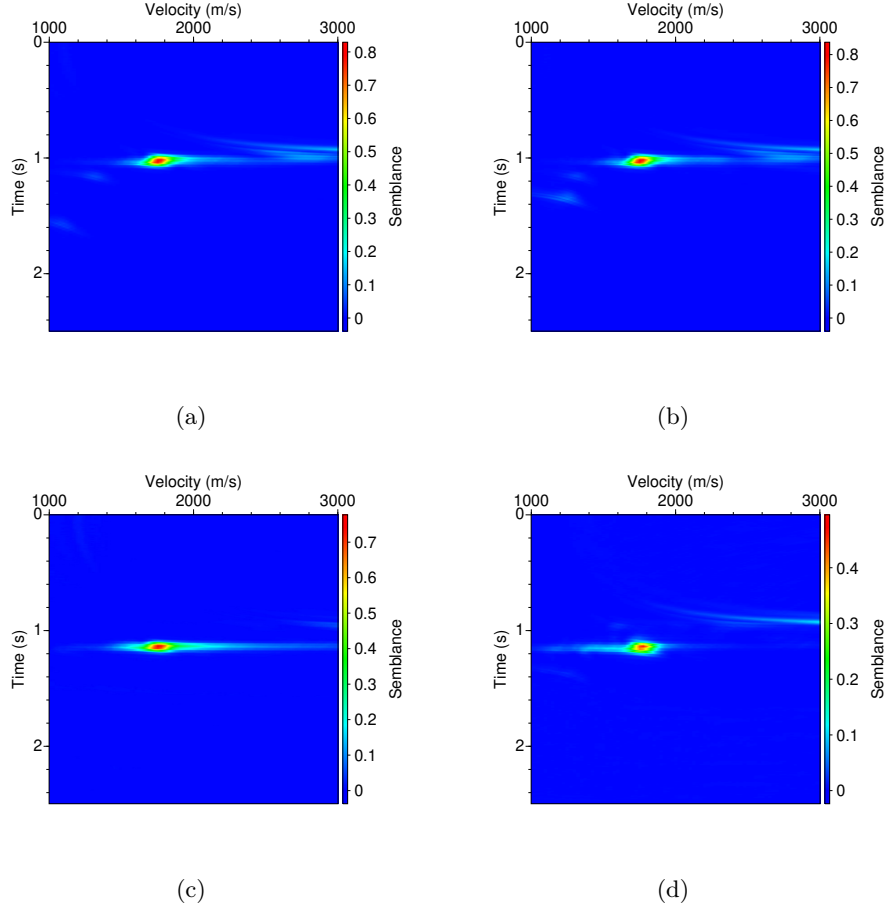


Figure 4: Results of time-migration velocity analysis for model A. (a-d) Time-migration velocity panels for CMP's for line C. Line C is directly above the diffraction apexes (a-c). The high value of semblance indicates the velocity is correctly determined for every diffraction. (d) Velocity panel for a CMP of line E. Here, the diffraction apex is located 60 meters outside of the profile, thus, semblance is not so high.

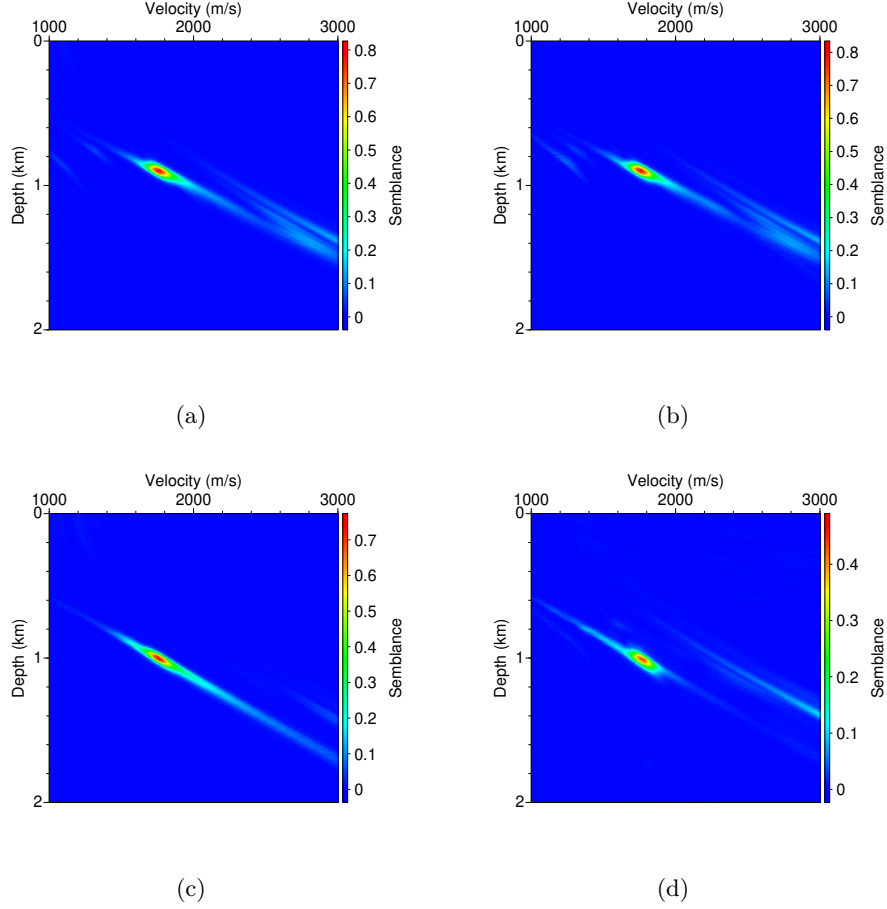


Figure 5: Results of depth-migration velocity analysis for model A. Depth-migration velocity panels for CMP's of the line C (see Figure 2(a)). The estimated depth velocity is an effective medium velocity. The high value of semblance indicates that the computed traveltimes match the data well.

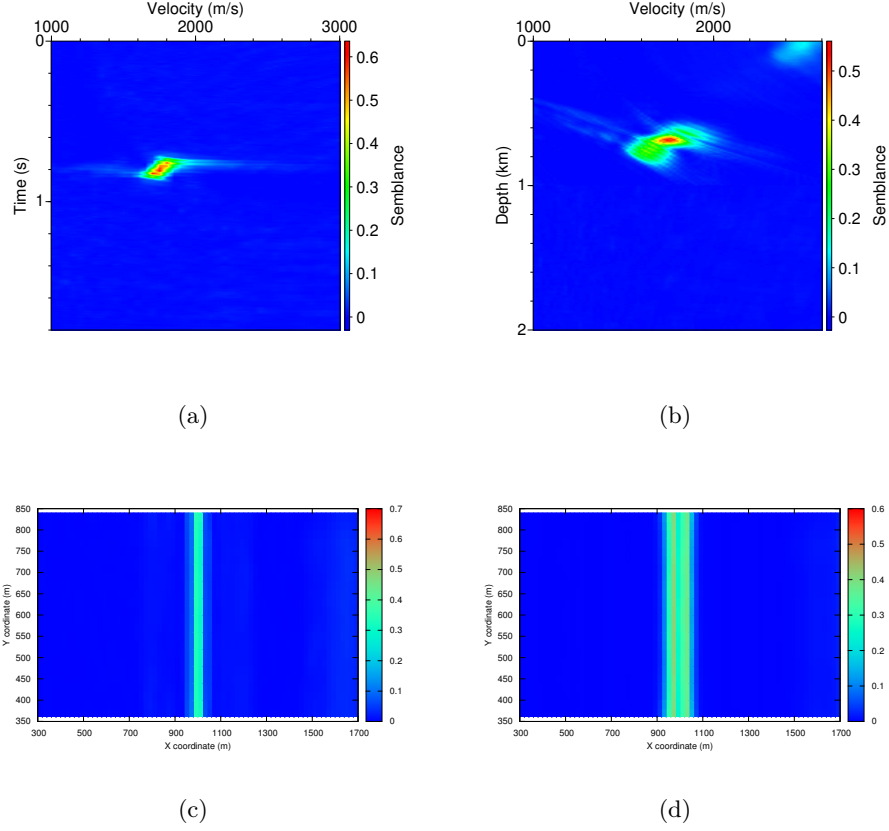


Figure 6: Results of migration velocity analysis for a vertical profile which is located at the middle of the stacked volume. (a) Time-migration velocity panel. The velocity panel is shown for the CMP which is directly above the edge. The high value of semblance indicates that the velocity is consistent with the data. (b) Depth-migration velocity panel for the same CMP. (c) Time slice through semblance cube at 0.8 s displayed as a function of lateral position for the determined time-migration velocity. We observe that the coherence maximum coincides with the lateral position of the edge. (d) Depth slice through the semblance cube at 700 meters plotted as a function of lateral position for the estimated depth-migration velocity. We observe that the coherence maximum coincides with the lateral position of the edge.



Figure 7: Sketch illustrating the geographic location of the study area (denoted by a red star) close to the czech border. The 3-D seismic dataset was acquired in the context of a geothermal exploration campaign near a small town called Schneeberg.

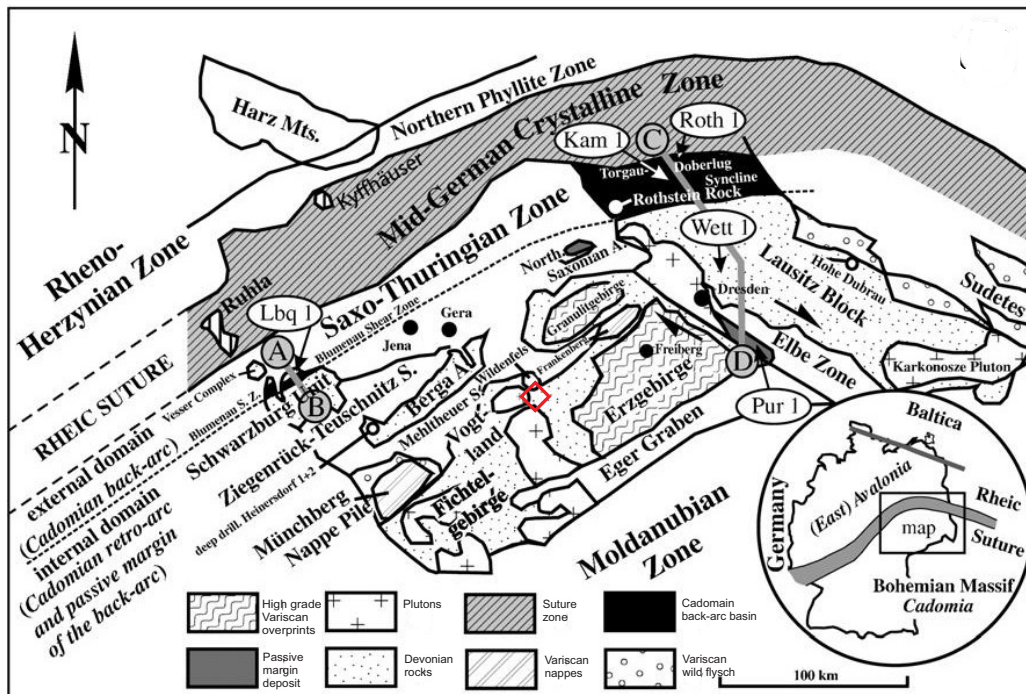


Figure 8: Tectonic map of Saxothuringian zone hinting at the overall structural complexity of the area under investigation. Aside from different localized units, the mid-German crystalline zone outcrops in the north of the acquisition (whose location is sketched by a red frame). Linnemann (2010)

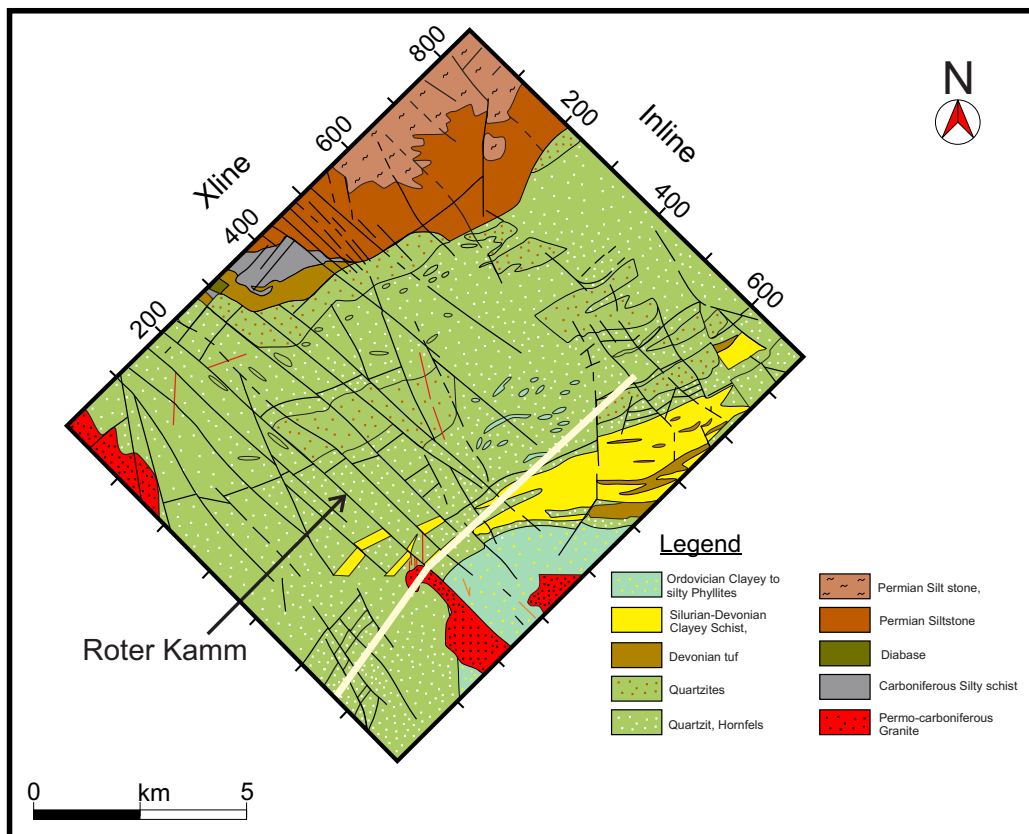


Figure 9: Geological map of the outcropping geology in the study area. Different colors indicate the different present geological units and a richness in fault systems is indicated by straight black lines. A main fault cutting through these formations (called *Roter Kamm*) is denoted by an arrow. H. J. Berger et al. (2011)

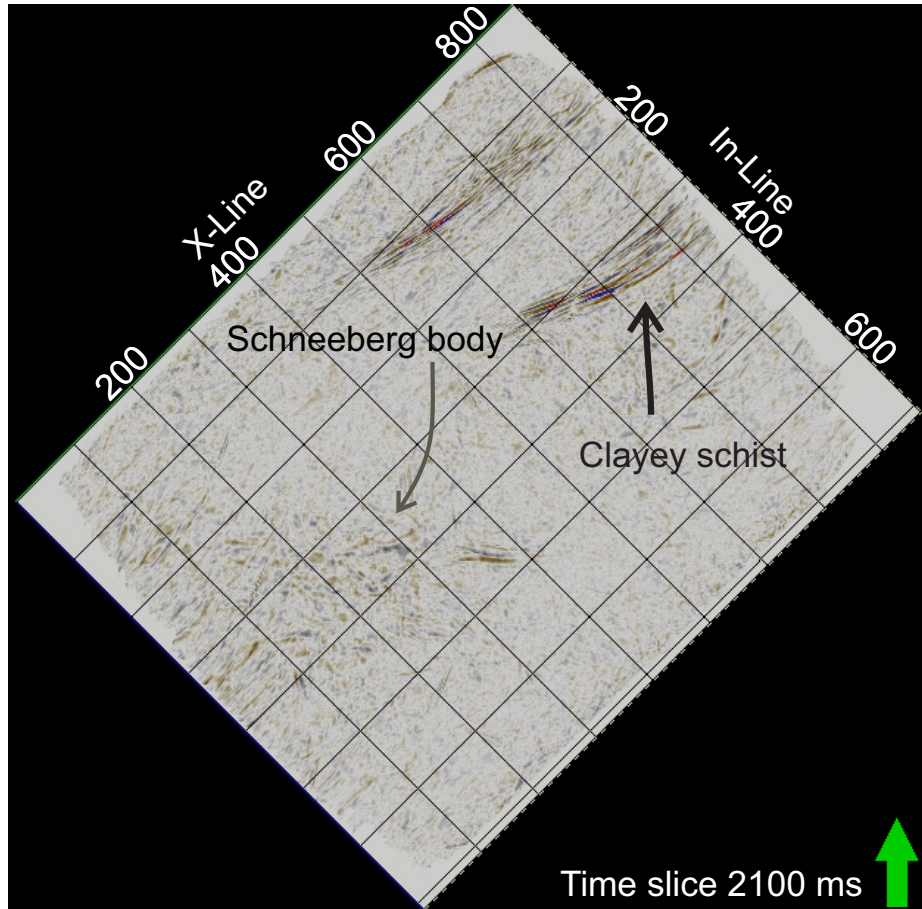


Figure 10: Time slice of the common-reflection-surface (CRS) stack (Ahmed et al., 2015). Arrows indicate the comparably strong signatures of the conjugate fault system known from outcrops related to mining and an apparently strongly diffracting structure (*Schneeberg body*).

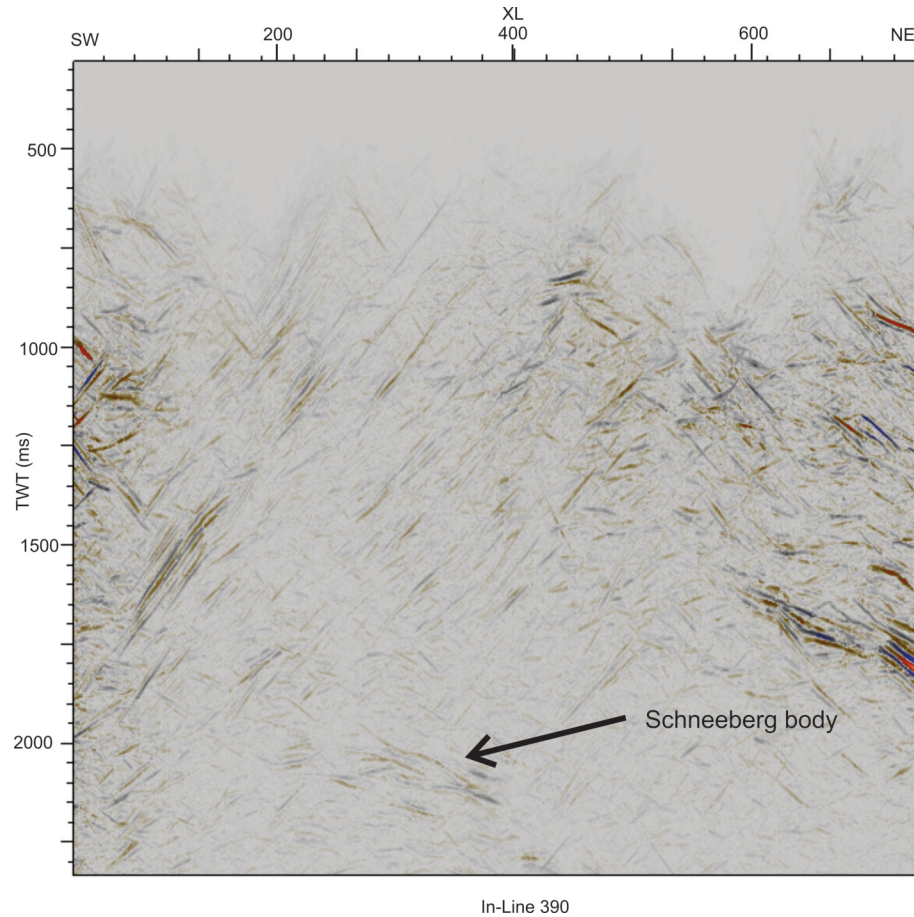


Figure 11: Inline 390 of the common-reflection-surface (CRS) stack of the 3D seismic dataset acquired for geothermal exploration (compare Ahmed et al., 2015). Like in Figure 10 both, the reflective likely mineralized conjugate fault structures and the seemingly highly diffractive *Schneeberg body* are clearly distinguishable.

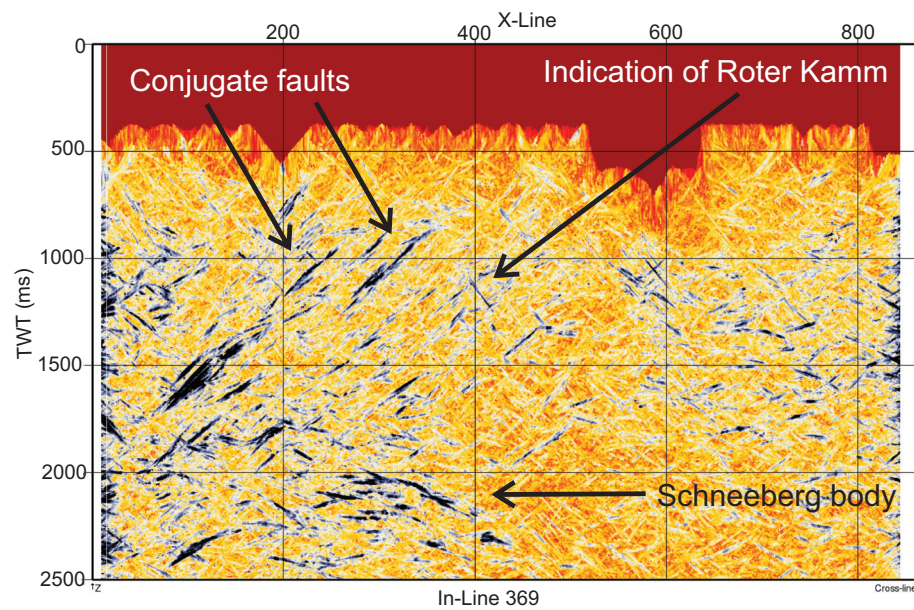


Figure 12: Maximized coherence achieved in the common-reflection-surface (CRS) workflow, indicating that aside from clearly distinguishable reflections caused by the minaralized faults near the surface, a stong variety of weak but coherent conflicting contributions could be detected throughout the dataset.

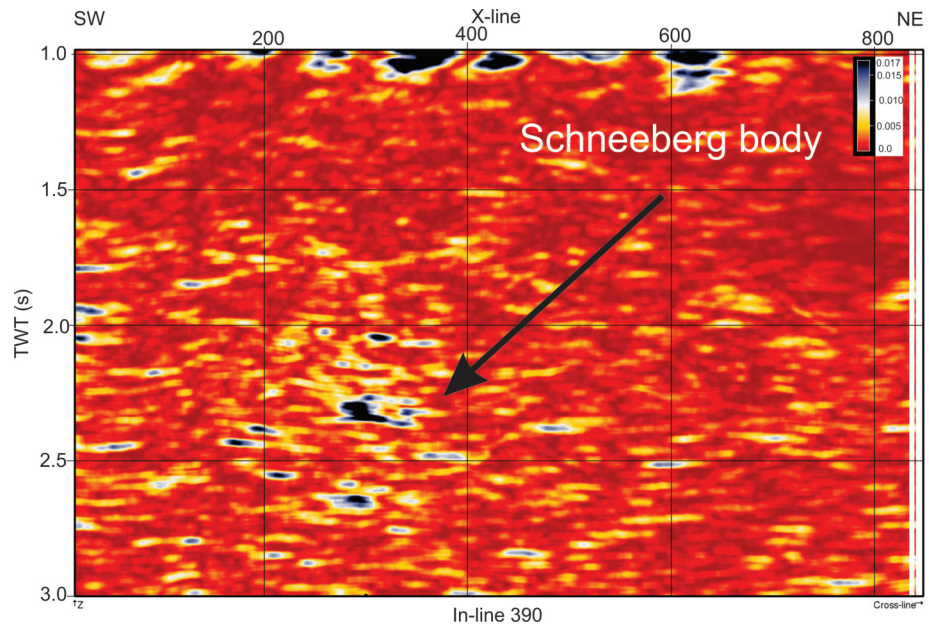


Figure 13: Result of the proposed data-driven diffraction focusing analysis shown for the central inline 390 (compare 11). Localized coherence peaks correspond to diffracted events focused at their apices.

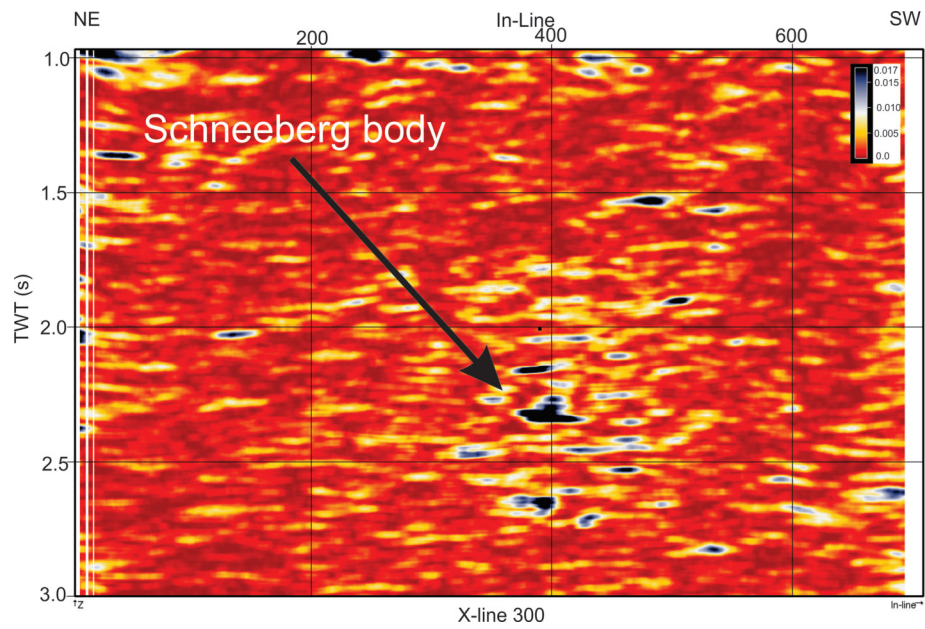


Figure 14: Exemplary crossline result (shown is crossline 300) of the suggested coherence-based scheme for diffraction focusing (compare Figure 13). While some noticeable diffractivity could be detected close to the surface, a majority of focussed energy seems to be related to the *Schneeberg body* structure.

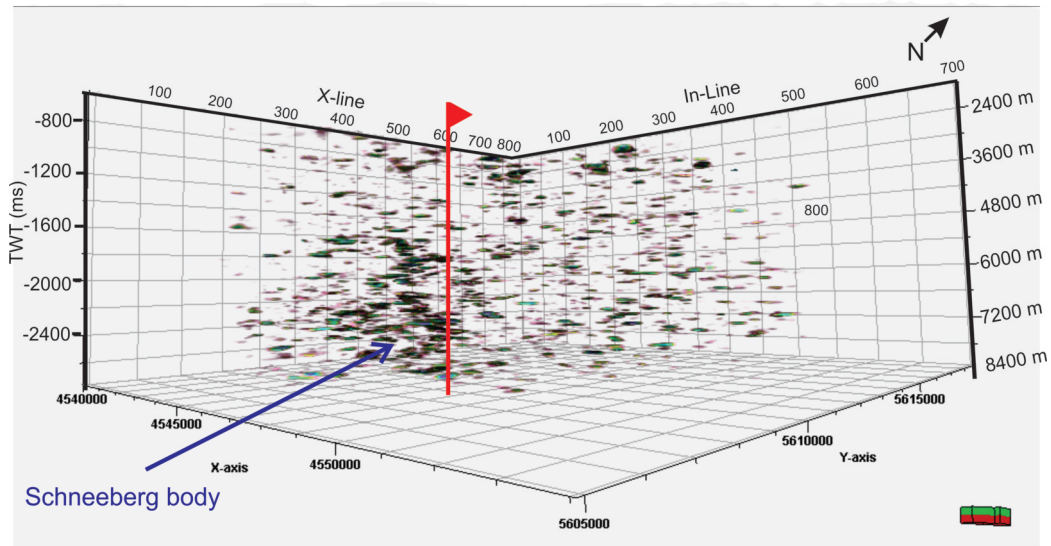


Figure 15: Full 3D visualization of the diffraction focusing achieved through the proposed workflow (low semblance values are transparent). While an overall diffractivity of the crystalline rocks can be observed, a higher diffraction rate in the location of the *Schneeberg body* hints at this structure's intrinsic complexity.